

Sintering Behaviour, Graded Microstructure and Corrosion Performance of Sintered Fe-Mn Biomaterials

Miriam Kupková^{1,*}, Monika Hrubovčáková¹, Martin Kupka², Renáta Oriňáková³,
Andrea Morovská Turoňová³

¹Institute of Materials Research, Slovak Academy of Sciences, Watsonova 47, SK-040 01 Košice, Slovak Republic

²Institute of Experimental Physics, Slovak Academy of Sciences, Watsonova 47, SK-040 01 Košice, Slovak Republic

³Department of Physical Chemistry, Institute of Chemistry, Faculty of Science, P.J. Šafárik University, Moyzesova 11, SK-041 54 Košice, Slovak Republic

*E-mail: mkupkova@imr.saske.sk

Received: 22 July 2015 / Accepted: 19 September 2015 / Published: 30 September 2015

This article discusses the corrosion of sintered Fe-Mn alloys, as influenced by spatial variability in microstructure and composition. Materials of interest were manufactured by mixing an iron powder with 25, 30 and 35wt.% of manganese powder, pressing the mixtures in a die and sintering. Particles that the sintered materials were comprised of possessed ferritic/martensitic core regions and austenitic peripheries. While the thickness of austenite shell seemed to increase with increasing Mn content for Fe-25Mn and Fe-30Mn materials, it appeared to fall to its lowest value for the Fe-35Mn material. The corrosion potential of a material exposed to Hank's solution increased with increasing Mn content for Mn-poorer materials but fell to its lowest value for the Mn-richest material. The fractal dimension of an electrochemical noise generated in corroding material was much lower than 1.5 for Mn-poorer materials but increased to the "white noise" value of 1.5 for the Mn-richest material. Corrosion rates of all materials were higher than those reported for homogeneous Fe-Mn alloys. It was concluded that while the Mn-richest material was very likely undergoing general corrosion, Mn-poorer materials suffered from galvanic interaction between particle cores and peripheries and their corrosion was dominated by localized events.

Keywords: biodegradable Fe-Mn sintered materials, corrosion, OCP, fractal dimension

1. INTRODUCTION

Metals and alloys possess an excellent combination of stiffness, strength and toughness, they can be made sufficiently chemically inert and stable, and the processes used to shape them are

relatively simple. That is why the metals and alloys are commonly used in fabricating medical devices which replace the missing structural components of the human body, which mechanically support the weakened tissues acted on by loads, etc..

As regards implants the presence of which is needed permanently, such as hip and knee joints, it is highly important to minimize their corrosion. But there are situations, e.g. the treatment of coronary artery occlusion, where the aid of an implant is needed only temporarily.

To fix the problem of narrowed arteries, metallic stents are widely used. A small tubular mesh-like structure—stent—is fabricated in a crimped form, transported into a blockage in an artery and then expanded. Afterwards the expanded stent holds the artery open.

The scaffolding function of the stent is needed only temporarily, usually no more than 24 months after stent implantation, a period during which the vessel remodels and heals. After the regeneration process is complete, the continuing presence of a foreign object in the arterial wall becomes detrimental to this wall and can trigger late complications. So, the short-term stents that are able to decompose in situ into harmless products which are absorbed by the human body and then readily excreted from it would be a better solution than the currently-used permanent stents [1]. Biodegradable metals and alloys which consist of trace elements existing in the human body are good candidates for temporary-stent's materials [2,3,4,5].

Pure iron stents were implanted into various mammals [6]. There was no evidence for the harmful effects of stents themselves or of products of their decomposition. However, stents remained almost intact for up to a year after implantation. This, and the modest mechanical properties of a pure iron have led to an attempt to make matters better by alloying the iron.

Hermawan et al. prepared Fe-Mn alloys with the manganese content ranging from 20 to 35 wt.% by a powder metallurgy route from elemental Fe and Mn powders. After several cold rolling-resintering cycles, the samples with more than 30wt.% of Mn possessed an austenitic structure and exhibited mechanical properties comparable to those of 316L stainless steel [1,2,3]. When immersed in a modified Hank's solution, the Fe-Mn samples corroded about 2.5 times more rapidly than a pure iron.

Though the mechanical characteristics met the requirements, degradation rates of Fe-Mn alloys were still considered too low for practical applications. In that context, new biodegradable alloys were developed by adding other elements, e.g. Fe–Mn–Pd, Fe-Mn-C-Pd [7], Fe-Mn-Si [8].

An alternative way of accelerating the degradation is to distribute the manganese non-uniformly, in contrast to the almost uniform distribution of Mn within the Hermawan's binary Fe-Mn systems. Due to chemical and/or phase composition varying on small scales, ground and polished surface of a material can be considered as comprised of many tiny spots of “dissimilar metals“ in electrical contact, which in the presence of an electrolyte yields many additional micro-galvanic cells initiating and accelerating corrosion.

Some preliminary results obtained for Mn-poorer alloys were published in [9]. This contribution deals also with PM Fe-Mn alloys with higher Mn contents. The objective of this study was to investigate the effect of spatially varied chemical composition and graded structure on corrosion properties. The effect on mechanical properties is the subject of future studies.

2. MATERIALS AND METHODS

Examined samples were prepared from elemental iron and manganese powders. Iron powder (Höganäs, water-atomized ASC 100.29 grade) and manganese powder (Alfa Aesar GmbH & Co KG, APS <10 micron, 99.6%) were mixed in a turbula mixer for 20 minutes. The mixtures with the Mn powder contents of 25wt.%, 30wt.% and 35wt.% were prepared. The powder mixtures were cold pressed in a die at 600 MPa into cylindrical compacts (Φ 10mm, h 10mm). No lubricant was used.

The compacts were then isothermally sintered in a laboratory tube furnace ANETA. The hold time at the sintering temperature of 1120°C was 60 minutes. The heating and cooling rate was kept at 10°C/min. The compacts were sintered in the atmosphere that consisted of 10% H₂ and 90% N₂ (purity 5.0). The flow-rate of the processing atmosphere was 4 l/min. The atmosphere was dried by the use of zeolite molecular sieve dryers. The inlet dew point (monitored by the SHAW Super-Dew Hygrolog) was about -59°C. Compact density values before and after sintering were obtained by weighing the compacts and measuring their dimensions.

All specimens were ground and further polished with 0.1 μ m diamond paste. Samples for metallographic analysis were also etched in 2% nital solution. To examine the microstructure of specimens, optical microscope (OLYMPUS GX71, Japan) and scanning electron microscope coupled with the energy dispersive spectrometer (JEOL JSM-7000F, Japan with EDX INCA) were used.

Corrosion of samples in Hank's solution was investigated. To simulate body fluids, solution composed of (in g/l) 8.00 NaCl, 1.00 Glucose, 0.60 KH₂PO₄, 0.40 KCl, 0.35 NaHCO₃, 0.14 CaCl₂, 0.10 MgCl₂ 6H₂O, 0.06 MgSO₄ 7H₂O, and 0.06 NaH₂PO₄ 2H₂O with a pH value of 7.4 was used. Measurements were carried out in a conventional three-electrode setup with the potentiostat Autolab Potentiostat PGSTAT 302N. The Ag/AgCl reference electrode, platinum counter electrode and iron or iron-manganese sample as the working electrode were used. The temperature of electrolyte was maintained at 37°C \pm 1°C. The samples were kept immersed in the electrolyte for 1 hour and the temporal evolution of the open-circuit potential (OCP) was recorded at first. After an hour the potentiodynamic measurements started. An external potential was applied and varied from -800 mV up to -200 mV at the scan rate of 0.1mV/s to obtain the polarization curves. The recorded OCP time series seemed to be a bit jagged. To probe whether they were fractals and to estimate their fractal dimension, the Higuchi's algorithm was used. Tafel slopes, corrosion currents, corrosion potentials and corrosion rates were determined from polarization curves by the use of the Tafel extrapolation technique.

3. RESULTS AND DISCUSSION

3.1 Microstructure of sintered materials and processes underlying its formation.

Upon sintering, the compacts from pure Fe powders shrank and compacts from mixed Fe and Mn powders swelled (Tab. 1). The Fe compacts shrank only slightly in diameter but markedly in height. For compacts from Fe-Mn mixtures, the relative elongation of height was nearly the same as

that of diameter. A decrease in mass of Fe samples was observed, while the mass of Fe-Mn samples increased.

The mass of pure iron compacts has decreased due to a reduction of oxides covering the surface of iron powder particles in the compact. Fe-Mn samples, on the other hand, have got heavier due to oxidation during sintering. The reason for this was a high affinity of manganese for oxygen, and a trace water vapour existing in the real sintering atmosphere served as a source of oxygen.

During sintering, a one-component iron powder compact has tried to lower down its free surface energy. This was causing the reduction of the total surface area of interparticle voids, shrinkage and elimination of pores, thereby reducing the compact's volume. The reason for the shrinkage anisotropy was that the compact's microstructure possessed a directionality of properties, resulting, e.g., from the decrease in "sphericity" of powder particles and from their alignment during the uniaxial pressing in a die [10,11]

As regards swelling of two-component Fe-Mn powder compacts, this was caused by diffusion of Mn atoms into Fe particles. During sintering, manganese sublimed from source particles, manganese vapour expanded into voids and deposited on the nearly whole available surface of iron particles. Manganese atoms then diffused into the Fe matrix and formed a solid solution with Fe, expanding thus original iron particles. These processes resulted in the observed macroscopic expansion [12].

Table 1. Changes in dimensions, changes in weights and resultant density of sintered compacts.

Material	Change of height $\Delta h/h$ [%]	Change of diameter $\Delta \Phi/\Phi$ [%]	Change of mass $\Delta m/m$ [%]	Density after sintering [g/cm ³]	Total porosity [%]
Fe	- 0.176	- 0.008	- 0.123	6.69	14.5
Fe-25Mn	+ 4.700	+ 4.623	+ 1.071	5.54	28.7
Fe-30Mn	+ 5.154	+ 5.070	+ 2.073	5.41	29.8
Fe-35Mn	+ 5.787	+ 5.662	+ 1.028	5.26	31.7

Taking into account the sintering temperature (1120°C), the hold time at the peak temperature (3600 s), the frequency factor ($0.35 \times 10^{-4} \text{ m}^2\text{s}^{-1}$ [13]) and the activation energy of diffusion of a manganese into a face-centered cubic iron matrix (282kJ mol^{-1} [13]), a mean displacement of a manganese from the surface towards the centre of an iron particle is estimated to be about $3\mu\text{m}$. Typical iron particles were several teens of microns in diameter. So, the manganese was diffusing into iron particles during the sintering step, but its concentration was spatially varied throughout a typical particle when the cooling started.

Upon usual cooling from a temperature well above 912°C to the room temperature, even Fe-Mn alloys with evenly distributed elements may exhibit quite complex microstructures. Alloys with Mn contents up to 11 wt.% represent substitutional solid solutions of a manganese in a body-centered cubic iron matrix and exhibit microstructures consisting of domains of ferrite (unsaturated or saturated

solid solution) and/or α' -martensite (supersaturated solid solution). For Mn contents over 28 wt.%, iron-manganese alloys show only a cubic close-packed solid solution phase (austenite) in which iron and manganese ions occupy at random regular sites of a face-centered cubic lattice. Fe-Mn alloys containing from 11 to 28 wt.% of Mn exhibit complex microstructures consisting of α' -martensite, hexagonal close-packed ϵ -martensite and austenite domains [1,14,15].

As a result, the sample preparation procedure has transformed previously fully ferritic iron particles into ones with a more (Fe-25Mn, Fe-30Mn) or less (Fe-35Mn) distinct onion-like structure – a core with a BCC structure surrounded by a layer comprised of many tiny grains and covered with an austenitic outer layer with a FCC structure (Fig. 1). The concentration of Mn increased from the particle core towards its periphery, and even free manganese was observed on the particle's boundary (Fig.1). Residues of original manganese particles have possessed forms of agglomerates and were composed of manganese, manganese oxide and a small amount of manganese sulphide, as the SEM+EDX analyses showed. The EDX analysis also revealed the presence of oxygen (Fig.2). This demonstrates a considerable oxidation during sample processing even when a high purity sintering atmosphere was applied.

For Fe-35Mn specimens, the fine-grain layer between the particle core and an austenitic shell was a bit different – grain boundaries were unclear and less visible, the oxygen content was lower too. The austenite outer layer was much thinner than expected on the basis of an original Mn content.

A mass increment and microstructural details of Fe-35Mn material have departed from the trend indicated by the remaining samples, most likely because of the compact became permeable during the sintering step when its porosity reached the percolation threshold [16,17].

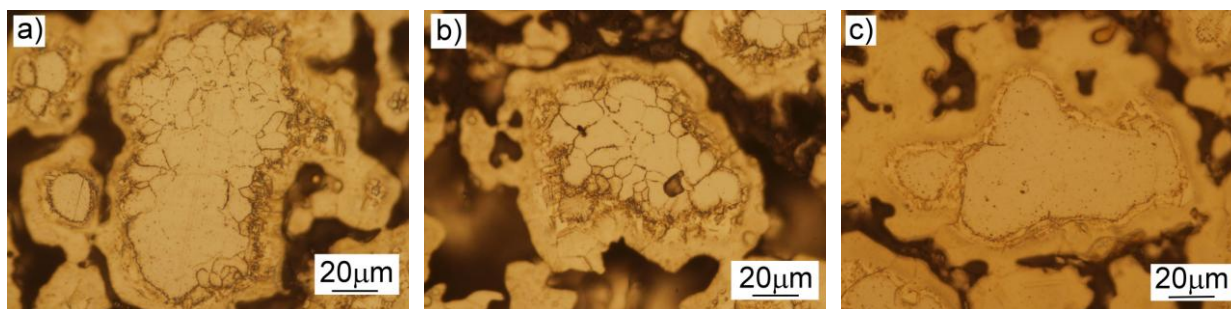


Figure 1. Optical micrographs of polished and etched sections of Fe-25Mn (a), Fe-30Mn (b) and Fe-35Mn (c) sintered alloys.

Within a continuum percolation model generated by creating identical convex cavities in a solid matrix, with centres distributed at random, the flow through the ensemble of cavities is possible if the porosity exceeds the critical value [16]

$$P_c = 1 - \exp \left[-B_c \frac{V}{\langle V_{ex} \rangle} \right] . \quad (1)$$

Here V represents the volume of a single pore, V_{ex} is the excluded volume surrounding a pore, i.e. a volume in which the centre of another pore cannot be located without overlapping, and $\langle V_{ex} \rangle$ means the excluded volume averaged over all possible orientations of intersecting pores. B_c is the averaged critical number of pores overlapping a typical pore. Numerical investigations have shown that the value of B_c is invariant for a variety of convex shapes of pores and is about 2.8 [18]. For spherical pores, the excluded volume is given by $\langle V_{ex} \rangle = 8V$, and so the critical porosity is about 0.295.

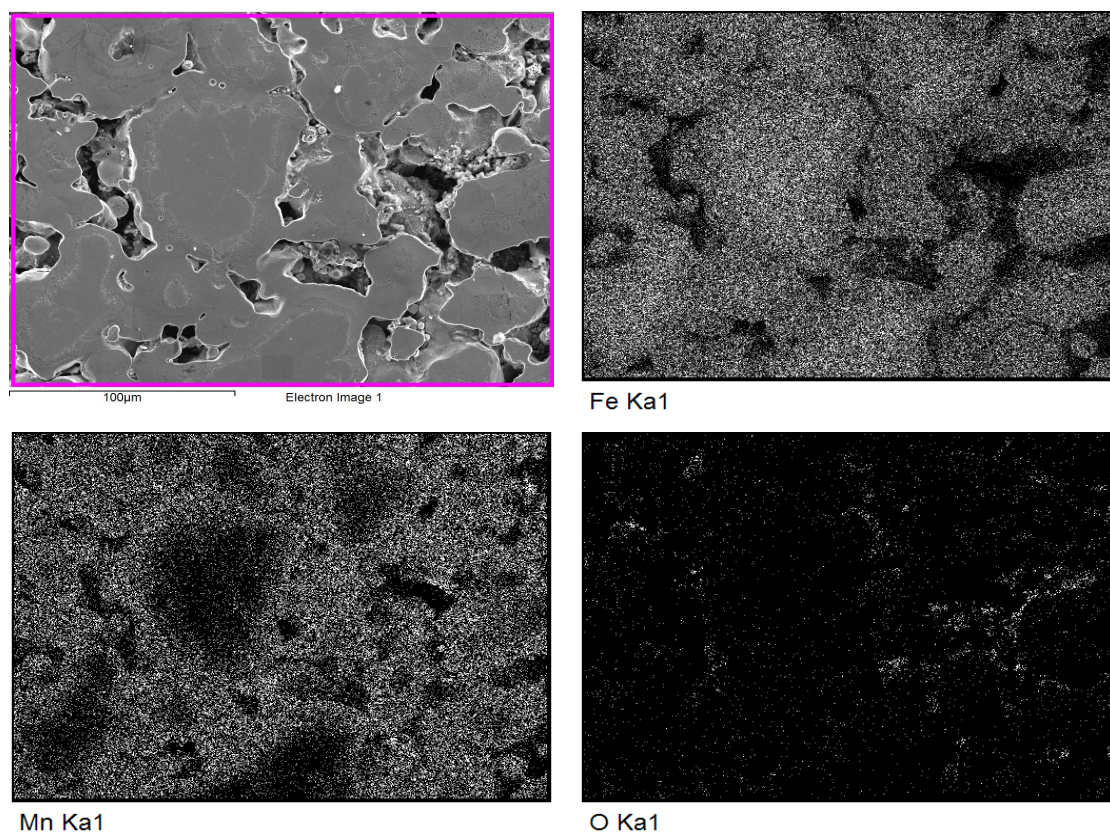


Figure 2. A scanning electron micrograph of a polished section of Fe-25Mn sintered compact and the EDX mapping of the distribution of iron, manganese and oxygen over this section.

The onset of macroscopic connectivity of pores during sintering enabled manganese vapour (and other gases) to escape from inside the sample into surroundings, which changed physical and chemical conditions within the sample. This could explain the lower mass increase for Fe-35Mn samples and might lead to differences in microstructure and thus also in property profiles exhibited by samples with the porosity below and above the percolation threshold.

3.2. Corrosion in Hank's solution

Studies of the degradation of sintered Fe-Mn alloys by Hank's solution began with a passive monitoring without external polarization. Figure 3 shows how the open-circuit potentials of the tested electrodes varied with passage of time.

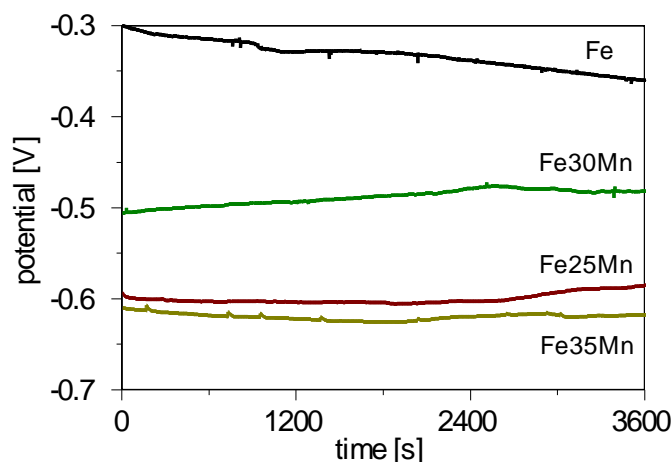


Figure 3. Variation of open-circuit potential with time measured on Fe, Fe-25Mn, Fe-30Mn and Fe-35Mn electrodes immersed in Hank's solution.

The highest open-circuit potential was that of the Fe electrode, and the potential of the electrode from Fe-35Mn was the lowest one. The potential of Fe-25Mn electrode was slightly above that of Fe-35Mn electrode, but the corrosion potential of Fe-30Mn electrode was shifted markedly to more positive values, in spite of the Mn content (Fig. 3). A possible explanation for such a behaviour of corrosion potential is that galvanic processes have taken place between different, large on the microscopic scale areas of an electrode comprised of several phases and that the cathode-anode area ratio was different for different materials.

The metallographic examination of corroded sections revealed a preferential corrosion attack on the core regions of particles while the austenitic rims remained almost unaffected. This implies a possibility of galvanic interaction between the particle's core and its periphery. The regions of electrode with the BCC structure (particle cores) acted as the anode and the regions with the FCC structure (particle peripheries) acted as the cathode. This spatial variability in electrochemical properties is illustrated in Figure 4. The micrographs, which were taken after exposing the electrodes to copper sulphate solution, show a selective deposition of copper on the periphery of particles. This demonstrates that the peripheral region is more cathodic than the core of particles (see, e.g. [19]).

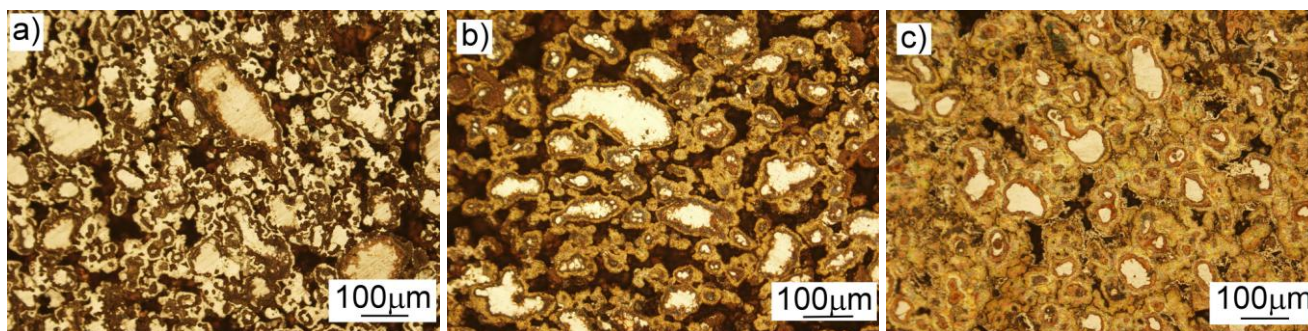


Figure 4. Scanning electron micrographs of sections of Fe-25Mn (a), Fe-30Mn (b) and Fe-35Mn (c) alloys after immersion in a CuSO_4 solution. The micrographs show selective deposition of copper on the more cathodic peripheral regions of particles.

Electrochemical parameters of an electrode undergoing galvanic corrosion are functions of the anode-cathode area ratio. If all anodic and cathodic polarizations of materials/phases the electrode is comprised of exhibit a Tafel behaviour, the mathematical analysis [20,21,22] provides the following expression for the corrosion potential:

$$E_{corr} = a + b \log \frac{A_{cathode}}{A_{anode}}, \quad b > 0. \quad (2)$$

Here $A_{cathode}$ (A_{anode}) is the surface area of the cathodic (anodic) region of the exposed surface of the examined electrode. Quantities a and b depend on the corrosion potentials and corrosion current densities of “anode” and “cathode” materials alone as well as on the Tafel slopes of their polarization curves, but they are independent of the areas of anode and cathode.

So, when the austenite-to-ferrite plus martensite ratio increases, the corrosion potential shifts towards more positive values. When this ratio decreases, the corrosion potential shifts towards more negative values.

When the variations of open-circuit potentials with time are observed with resolution no better than centivolt, the OCPs recorded for Fe-Mn electrodes appear to be quite smooth functions of time, with positive-going or negative-going potential transients occurring from time to time (Fig.3). These sharp, several-centivolts increases or decreases in potential which decay in an exponential-like way over a short time period were caused by localized short-lived mesoscopic corrosion events, such as an initiation and propagation of a crack (stress corrosion cracking), initiation and penetration of a pit (pitting corrosion), etc.. But when we look closer, on a finer scale, open-circuit potential vary from instant to instant quite irregularly and unpredictably. This gives rise to a rather jagged OCP time series with a more or less irregular structure. When considered as a subset of the (time, potential)-coordinate plane, such OCP time series may be a fractal. To examine the possibility that OCP time series are fractals and to estimate corresponding fractal dimensions, the Higuchi's method was used.

The Higuchi's estimator [23] was chosen as some of authors have a good experience with the use of this method, e.g., for investigation of the wear process [24,25] or recently for determining fractal characteristics of an electrochemical noise generated in a corroding Fe-P system [26]. It is one of the most robust method which enable one to compute the fractal dimension of discrete time series and which provides the most accurate estimates of this dimension [27]. The algorithm is briefly sketched below.

Let $X(1), X(2), \dots, X(N)$ be the time sequence to be analysed. From this time series, following k new time series X_m^k are constructed:

$$X_m^k = \{X(m), X(m+k), X(m+2k), \dots, X(m+n_{li}(N, m, k)k)\} \quad \text{for } m=1, 2, \dots, k. \quad (3)$$

Here $n_{li}(N, m, k)$ represents the lower integer part of $(N-m)/k$. m indicates the initial value of time, and k stands for the discrete time interval (delay) between points. For a time interval equal to k ,

one gets k sets of new time series. For each of the time series X_m^k , the length of the “curve” is defined as follows:

$$L_m(k) = \frac{N-1}{n_{li}(N,m,k)k^2} \sum_{i=1}^{n_{li}(N,m,k)} |X(m+ik) - X(m+(i-1)k)|. \quad (4)$$

The term $(N-1)/n_{li}(N,m,k)k^2$ serves as the normalization factor for the curve length of subset time series. For the time delay k , the length $\langle L(k) \rangle$ of the curve is defined as the average value of k lengths $L_m(k)$. If $\langle L(k) \rangle \propto k^{-D}$, then the analysed curve is a fractal and its fractal dimension is D .

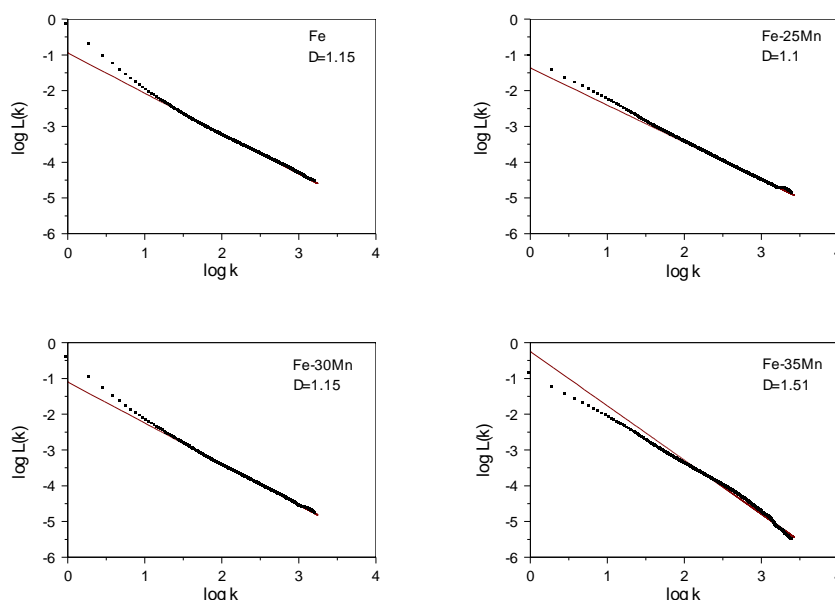


Figure 5. The results provided by the Higuchi's estimator applied to OCP time series. Here k represents the discrete time interval between points that constitute a particular subset of the time sequence being analysed. $L(k)$ is the average value of the length of the OCP time subseries defined by the discrete time step k . D represents the corresponding fractal dimension of the OCP time series.

Figure 5 shows the results that the “fractal geometry” analysis has provided for the records of temporal evolution of the OCPs of investigated electrodes. It was found that for each of the tested samples the variations of open-circuit potential with time gave rise to a time series which was a fractal in the (time, potential)-coordinate plane with the fractal dimension $D > 1$. For Fe electrode $D = 1.15$, for Fe-25Mn electrode $D = 1.1$, for Fe-30Mn electrode $D = 1.15$, for Fe-35Mn electrode $D = 1.51$.

When a metallic electrode is undergoing the simplest case of corrosion, a lot of microscopic corrosion cells are distributed at random over the surface of the corroding electrode. Anodic and cathodic sites „wander“ irregularly from instant to instant from one place to another one. The overall effect is the uniform corrosion [28]. The corrosion potential is thus a result of the superposition of contributions from numerous more or less independent surface corrosion events. The resultant temporal evolution of open-circuit potential of the uniformly corroding electrode may be therefore

considered as a particular realization of the stochastic Gaussian process. The Gaussian noise gives rise to a time series with a fractal dimension of 1.5 [29,30].

If the corrosion process is dominated by localized corrosion events, for example by pitting, with pits (anodic sites) located at imperfections in a seemingly uniform material or around the interface between noble and active regions of the electrode, the corrosion potential represents the superposition of contributions from corrosion events which tend to be positively correlated. The reason for the correlation is that existing pit raises the probability of the event that this pit will penetrate deeper in a later time, providing thus a potential transient of the same kind as during previous steps. So, the resultant corrosion potential fluctuates as though it was a fractional Gaussian noise with the Hurst exponent higher than 0.5. Such a noise yields a time series which is less jagged, with a lower fractal dimension that falls into the interval between 1 and 1.5 [29,30].

For the Fe-35Mn electrodes, the OCP time series were found to possess the fractal dimensions of about 1.50. This implies that those samples most likely undergo nearly uniform (or general) corrosion.

As regards Fe, Fe-25Mn and Fe-30Mn electrodes, the fractal dimensions of their OCP time series were clearly less than 1.5. So the corrosion of those electrodes seems to be localized.

After the OCP recording had finished, potentiodynamic polarization measurements were carried out. The corrosion potential (E_{corr}) and corrosion current density (i_{corr}) were evaluated from the intersection of the lines (anodic and cathodic) obtained by extrapolating the Tafel regions of polarization curves (Fig. 6). The corrosion rate (R_M) was calculated according to ASTM G 102-89 [31]. All values of b_a , b_c , Tafel slopes, E_{corr} , i_{corr} and R_M , are summarized in Tab.2.

Corrosion potentials determined from polarization curves (Fig. 6) agreed with those obtained from temporal evolution of open-circuit potentials (Fig. 3). The addition of a more active manganese to a nobler iron shifted the corrosion potential towards more negative values, that is, made the material more prone to corrosion. A quite noble corrosion potential of Fe-30Mn electrode, nobler than expected on the basis of its manganese content alone, is ascribable to galvanic processes occurring between different areas of the exposed surface of a given electrode, and to a higher ratio of cathodic surface area (austenite) to anodic surface area (ferrite, α' -martensite).

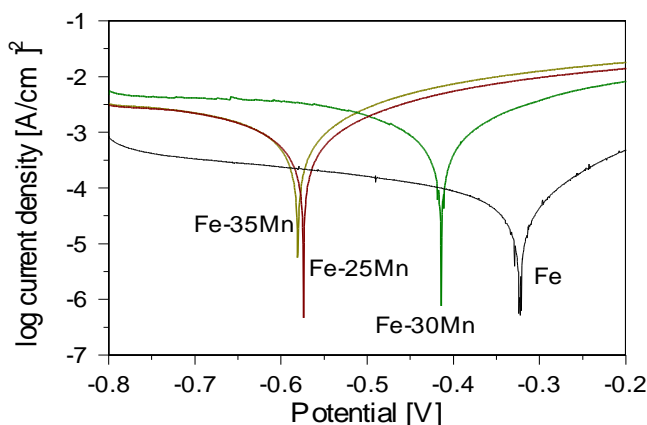


Figure 6. Polarization curves for iron and iron-manganese samples immersed in Hank's solution.

To evaluate the corrosion current densities and corrosion rates, it was assumed that the exposed electrode surface was attacked uniformly and no selective oxidation took place. When the localized corrosion processes were occurring, the obtained results underestimate the true value of corrosion rate and are only an approximate guide.

Table 2. Tafel slopes, corrosion potentials, corrosion current densities and corrosion rates of tested materials determined from polarization curves.

Sample	b_a [mV/dec]	b_c [mV/dec]	E_{corr} [mV]	i_{corr} [A/m ²]	Corrosion rate [mm/year]
Fe	43	51	-322	0.10	0.14
Fe-25Mn	32	32	-574	1.03	1.71
Fe-30Mn	36	32	-412	1.07	1.79
Fe-35Mn	32	30	-580	1.06	1.79

The corrosion current density (i_{corr}) obtained for the Fe sample was about ten times lower than i_{corr} measured for Fe-Mn samples. The corrosion current densities obtained for Fe-Mn samples were nearly equal each other and the difference in corrosion rates calculated from those data was not significant. The corrosion resistance of Fe samples was thus found higher than that of any Fe-Mn sample. But, as at least a part of samples was undergoing localized corrosion, the data concerning corrosion current densities and corrosion rates have to be treated as a qualitative, approximate guide.

In principle, Tafel slopes may enable one to gain information on the electrode reaction mechanism by comparing experimental data with values obtained for suitable models.

For instance, if an iron dissolves in a weakly acidic electrolyte at 37°C according to Bockris mechanism, the anodic Tafel slope of 41 mV per decade is calculated, while the mechanism proposed by Heusler provides the slope of 31 mV per decade [19]. Both mechanisms involve adsorbed OH⁻ ions taking part in a charge transfer reaction and FeOH_{ads} and FeOH⁺ occurring as reaction intermediates. The mechanism differs in a number of electrons transferred in the rate-determining step: the former mechanism assumes the transfer of one electron, the latter one assumes the simultaneous transfer of two electrons.

For most real, non-ideal electrodes, the polarisation curves are results of various simultaneous multi-step reactions of various rates and orders. So it is quite difficult to relate Tafel slopes to particular electrode reactions and such an analysis is outside the scope of this article.

4. CONCLUSIONS

Iron and iron-manganese specimens were prepared via the powder metallurgy route to study the effect of 25,30 and 35 wt.% of manganese powder admixed to the iron powder on the evolution of microstructure and on in-vitro electrochemical degradation of prepared materials in Hank's solution.

It was found that the property profile exhibited by the Fe-35Mn material departed from the trend the Fe-25Mn and Fe-30Mn materials had set. Significant findings are summarized below.

The oxygen from a trace water vapour existing in a furnace atmosphere was bound to a manganese. The mass of sintered Fe-Mn compacts was therefore higher than the mass of green compacts. The relative mass increment increased with increasing Mn content for Fe-25Mn and Fe-30Mn samples, but for Fe-35Mn samples the relative mass increment was the lowest one.

After sintering, originally ferritic iron particles were comprised of γ -(Fe,Mn) austenite shell and cores from ferrite and/or α' -martensite which possessed more or less spatially varied concentration of Mn. The thickness of the austenitic layer seemed to increase with increasing Mn content for Fe-25Mn and Fe-30Mn samples, but for the Fe-35Mn samples the austenitic shells looked the thinnest ones, the microstructure of cores was very fine and the chemical composition was quite uniform.

The alloying with Mn made the materials more prone to corrosion. Corrosion potentials of alloys were more negative than the corrosion potential of a pure iron. Corrosion potentials increased with increasing Mn content for Fe-25Mn and Fe-30Mn materials, but the corrosion potential of Fe-35Mn material was the most negative one.

The temporal evolution of open-circuit potentials of freely corroding electrodes yielded time series which were fractals. The fractal dimensions of OCP time series for Fe-25Mn and Fe-30Mn electrodes were low, much lower than 1.5, while the fractal dimension of the OCP time series for the Fe-35Mn electrode was about 1.5. So, fluctuations of corrosion potential generated in corroding Fe-25Mn and Fe-30Mn electrodes seemed to be positively autocorrelated, while the corrosion potential fluctuations generated in the Fe-35Mn electrode seemed to be uncorrelated.

Taking all these data together one finds that the Fe-25Mn and Fe-30Mn samples were very likely undergoing localized galvanic corrosion while Fe-35Mn samples corroded nearly uniformly.

As regards a reason for the above differences, it is assumed that Fe-35Mn compacts became permeable when their porosity reached a percolation threshold during the sintering step. The percolation threshold for the continuum percolation model with overlapping spherical pores is about 30%. The onset of macroscopic connectivity in a system of pores enabled manganese vapour and other substances to escape from the sample. This changed physical and chemical conditions inside the sample, which consequently affected the mass increment and the evolution of microstructure.

The non-uniform distribution of manganese indeed accelerated the corrosion. The corrosion rates obtained for sintered Fe-Mn alloys with graded microstructures were much higher than the rates reported for nearly uniform alloys [1]. However, as the samples were most likely undergoing non-uniform corrosion, the long-term weight-loss tests are needed to obtain more reliable data.

The verification of transition between porosity regimes below and above the percolation threshold, the effect of such a transition on the composition, structure and properties of sintered samples as well as the validation of the usefulness of the methods of fractal geometry for the analysis of corrosion phenomena are the subjects of future studies.

ACKNOWLEDGEMENTS

The authors thank for financial support of the research by the Slovak Research and Development Agency under contract APVV No. 0677-11 and VEGA grant 2/0100/15.

References

1. H. Hermawan, D. Dubé and D. Mantovani, *Acta Mater.*, 6 (2010) 1693
2. H. Hermawan, D. Dubé and D. Mantovani, *J. Biomed. Mater. Res.*, Part A 93 (2010) 1
3. H. Hermawan, A. Purnama, D. Dube, J. Couet and D. Mantovani, *Acta Biomater.*, 6 (2010) 1852
4. W.M. Hosny, M.A. Ameer, *Int. J. Electrochem. Sci.*, 8 (2013) 8371
5. Z. Wen, S. Duan, Ch. Dai, F. Yang and F. Zhang, *Int. J. Electrochem. Sci.*, 9 (2014) 7846
6. M. Peuster, C. Hesse, T. Schloo, C. Fink, P. Beerbaum and C. von Schnakenburg, *Biomaterials*, 27 (2006) 4955
7. M. Schinhammer, C.M. Pecnik, F. Rechberger, A.C. Hänzi, J.F. Löffler and P.J. Uggowitzer, *Acta Mater.*, 60 (2012) 2746
8. B. Liu, Y.F. Zheng and L.Q. Ruan, *Mater. Lett.*, 65 (2011) 540
9. M. Kupková, M. Hrubovčáková, A. Zeleňák, M. Sulowski, A. Cias, R. Oriňáková, A. Morovská Turoňová, K. Žáková and M. Kupka, *Arch. Metall. Mater.*, 60 (2015) 639
10. R.M. German, *Sintering: From Empirical Observations to Scientific Principles*, Elsevier Butterworth-Heinemann, Oxford (2014)
11. M.N. Rahaman, *Sintering of Ceramics*, CRC Press Taylor & Francis Group, Boca Raton (2007)
12. E. Hryha, E. Dudrová and L. Nyborg, *Metall. Mater. Trans. A*, 41 (2010) 2880
13. W.F. Hosford, *Iron and Steel*, Cambridge University Press, New York (2012)
14. Q. Peng, Ch. Song, W.Xia and Q. Zhai, in *TMS 2013 Annual Meeting Supplemental Proceedings* (John Wiley & Sons, New Jersey, 2013) pp. 869-875.
15. Y.K. Lee, J.H. Jun and Ch.S. Choi, *ISIJ Int.*, 37 (1997) 1023
16. B. Berkowitz and R.P. Ewing, *Surv. Geophys.*, 19 (1998) 23
17. I. Balberg, *Philos. Mag. B*, 56 (1987) 991
18. A.L. Efros, *Physics and Geometry of Disorder. Percolation Theory*, Mir Publishers, Moscow, (1986)
19. D. Landolf, *Corrosion and Surface Chemistry of Metals*, EPFL Press, Lausanne (2007)
20. R.W. Revie and H.H. Uhlig, *Corrosion and Corrosion Control. An Introduction to Corrosion Science and Engineering*, 4th ed., John Wiley & Sons, Inc. Hoboken, New Jersey (2008)
21. M. Stern, *Corrosion*, 14, (1958) 329t
22. F. Mansfeld, *Corrosion*, 27, (1971) 436
23. T. Higuchi, *Physica D*, 31 (1988) 277
24. M. Kupková, M. Kupka, E. Rudnayová and J. Dusza, *Wear*, 258 (2005) 1462
25. M. Kupková, M. Kupka, E. Rudnayová and J. Dusza, *Key Eng. Mater.*, 290 (2005) 276
26. M. Kupková, M. Hrubovčáková, M. Kupka, R. Oriňáková, A. Morovská Turoňová, *Int. J. Electrochem. Sci.*, 10 (2015) 671
27. P. Simard and E. La Tavernier, *Mech. Syst. Signal Pr.*, 14 (2000) 459
28. E. McCafferty, *Introduction to Corrosion Science*, Springer Science + Business Media, New York, (2010)
29. P.S. Addison, *Fractals and Chaos: An Illustrated Course*, IOP Publishing, Bristol, (1997)
30. D.L. Turcotte, *Fractals and Chaos in Geology and Geophysics* second edition, Cambridge University Press, Cambridge, (1997)
31. ASTM G102-89, *AST International*, West Conshohocken, PA (2010), www.astm.org